Additive Manufacturing 110 (2025) 104922

Contents lists available at ScienceDirect

Additive Manufacturing

journal homepage: www.elsevier.com/locate/addma

Laser powder bed fusion of an Fe-based metallic glass using time delays

M. Rodríguez-Sánchez [a,b,*], A.D. Boccardo [a,c], S. Sadanand [a,b], A. Ghavimi [d], R. Busch [d], P. Sharangi [e], E. Ferrara [e], G. Barrera [e], P. Tiberto [e], D. Tourret [a], I. Gallino [d,f], M.T. Pérez-Prado [a]

[a] IMDEA Materials Institute, Calle Eric Kandel, 2, Madrid, Getafe 28906, Spain
[b] Materials Science and Engineering Department, Universidad Carlos III de Madrid, Av. De la Universidad 30, Madrid, Leganés 28911, Spain
[c] Durability and Mechanical Integrity of Structural Materials group (DIMME), Universidad Rey Juan Carlos, C/Tulipán, s/n, Madrid, Móstoles 28933, Spain
[d] Saarland University, Institute of Metallic Materials, Campus C6.3, Saarbrücken 66123, Germany
[e] INRIM, Istituto Nazionale di Ricerca Metrologica, Strade delle Cacce, 5, Torino 10135, Italy
[f] Technical University of Berlin, Department of Materials Science and Engineering, Metallic Materials, Berlin, TU, Ernst-Reuter Platz 1, Berlin 10587, Germany

ARTICLE INFO

Keywords:
Laser powder bed fusion
Multiphysics finite element simulations
Fe-based metallic glasses
Time delays
Amorphous phase
Coercive field
Soft magnetics

ABSTRACT

Laser powder bed fusion (LPBF) of dense and fully amorphous commercial Fe-based metallic glass (MG) alloys, such as Kuamet 6B2, remains challenging when using simple scanning strategies. High-energy conditions produce dense but highly crystalline samples, while low-energy conditions led to higher amorphous fractions and reduced density. This study investigates the impact of introducing a controlled laser-off period ("time delay," t_{OFF}) after each scan track in an LPBF meander scanning strategy on the processability, density, crystallinity, and coercive field (H_c) of Kuamet 6B2 specimens. LPBF is performed using pulsed laser emission with two laser power levels (120 W and 160 W), two scan speeds (615 mm/s and 888 mm/s), and time delays ranging from 1 to 300 ms. Introducing time delays as short as 50 ms significantly increases the amorphous fraction (AM%) without compromising density and leads to notable decreases in H_c. Multiphysics finite element (FEM) simulations reveal that this increase in AM% results from reduced devitrification in the heat-affected zone, as amorphous regions solidified during the previous track are allowed to cool during t_{OFF}—an effect that becomes more pronounced with longer delays. This study demonstrates, for the first time, that implementing time delays can effectively resolve the "density/amorphous fraction" paradox in Fe-based MGs, providing a viable strategy for LPBF manufacturing of these alloys for soft magnetic applications.

1. Introduction

Since their discovery in 1960 [1], metallic glasses (MGs) have attracted much attention in the scientific community as their amorphous structure endows them with properties that, in many cases, are not commonly found on crystalline metals. Fe-based MGs, in particular, possess extraordinary soft-magnetic properties such as low permeability, high electrical resistivity, and low coercivity [2], which are highly sought-after for components of electrical motors like rotors or stators, as they contribute to reducing electrical losses, resulting in highly efficient machines [3,4]. As the global use of electrical motors keeps increasing and electrical energy is becoming an extremely valuable resource, significant efforts are being made in finding viable ways to commercialize these materials for industrial applications.

The major drawback hindering a wider commercialization of Fe-based MGs is their ease to crystallize upon cooling, which is higher than that exhibited by other alloy families such as Zr or Ti-based MGs [5]. The critical sheet thickness, t_c, or, alternatively, the critical rod diameter, d_c, are widespread metrics to assess the maximum dimensions that cast specimens can have without crystallizing. Fe-based MGs which are free of elements such as Co and rare earths typically present d_c between 0.1 mm and 5 mm [2]. Additionally, $d_c < 0.5$ mm is found in Fe-based compositions that are free of phosphorous, a highly volatile element. For instance, the commercial Kuamet 6B2 alloy has a t_c as low as 150 μm. These sizes are clearly insufficient to manufacture large components with complex shapes such as those required for industrial applications.

Since the cooling rate needed to produce fully amorphous Fe-based MG specimens is in the order of $10^5 - 10^6$ K/s [6], viable manufacturing routes have so far been limited to melt-spinning of thin ribbons [7], powder atomization [8], and suction casting of thin rods [9], and significant research has been devoted in the last decades to

---

* Corresponding author at: IMDEA Materials Institute, Calle Eric Kandel, 2, Madrid, Getafe 28906, Spain.
E-mail address: marcos.rodriguez@imdea.org (M. Rodríguez-Sánchez).

https://doi.org/10.1016/j.addma.2025.104922
Received 9 April 2025; Received in revised form 31 July 2025; Accepted 5 August 2025

design alloy compositions with improved glass forming ability (GFA) during casting processes [5]. Powder-based additive manufacturing (AM) techniques such as laser powder bed fusion (LPBF) have been recently put forward as promising avenues to fabricate large bulk metallic glass (BMG) parts, as the high local cooling rates following laser melting (10^5-10^7 K/s) [2,5,10–13] are of the same order of magnitude as those required for the stabilization of the amorphous phase in most MG systems. Furthermore, the design flexibility offered by LPBF allows manufacturing of components with intricate geometries, such as those required in highly efficient e-motors to reduce energy losses due to eddy currents and to effectively guide magnetic fields [14,15].

The AM processability of MGs has been mostly related to their GFA. LPBF manufacturing of dense components with a fully amorphous structure (within X-ray diffraction detection limits) has already been achieved in Zr-based [16–22], Ti-based [23], Cu-based [24] and Ni-based [25] MGs using simple scanning strategies, such as the widely used meander path with interlayer 67-degree rotations. However, if one uses Fe-based alloys with critical casting thicknesses that are much smaller than 1 mm, such strategies are in general not able to yield Fe-based BMG parts with both high density *and* high amorphous fractions for any combination of laser power and scan speed [10,11,13]. Indeed, previous works on LPBF processing of soft magnetic Fe-based BMGs have shown that high volumetric energy conditions can minimize porosity but cause much devitrification, which significantly increases the magnetic coercivity, while low volumetric energy combinations that favor the retention of the amorphous phase tend to result in lack of fusion porosity [26–36]. Therefore, dense Fe-based BMGs manufactured by LPBF using simple scanning strategies consist typically of glassy-crystalline composites [26–36], as crystallization unavoidably takes place following solidification during the thermal cycles resulting from the deposition of neighboring tracks or subsequent layers during LPBF. A breakthrough in LPBF processing of Fe-based BMGs involving advanced scanning strategies would be required to manufacture reliably complex geometry components with dense and fully amorphous structures that would enable a new generation of highly efficient motors with a drastic reduction of energy losses.

Sohrabi et al. [37] recently reported that the density and the amorphous fraction of an LPBF-manufactured Zr-based BMG could be simultaneously increased using conventional parallel single scanning strategies by the introduction of time delays (i.e., pre-defined time periods during which the laser is switched off) after each scan track. This approach reportedly mitigates crystallization at the turning points of the laser, where the dwell time is accumulated by the solidified material at high temperature peaks [38]. Studies on direct energy deposition (DED) of MGs have also shown that the implementation of time delays between printing tracks is a promising approach to reduce the temperature throughout the sample [39–41]. Finally, in LPBF of crystalline metals, time delays between layers [42] and at the turning points of printed tracks [43] have been used to homogenize the thermal profiles throughout the sample. To date, the introduction of time delays in LPBF manufacturing of Fe-based metallic glasses has not been explored.

The aim of this work is to investigate whether the introduction of time delays after each scan track would enable LPBF manufacturing of dense *and* amorphous Fe-based BMGs using a meander scanning strategy. To that end, LPBF is carried out using pulsed wave emission and a wide range of complementary characterization techniques is utilized to relate the defect structure, the fraction of amorphous phase, and magnetic coercive field (H_c) to the processing parameters on a commercial Kuamet 6B2 Fe-based soft magnetic MG alloy. Additionally, multiphysics finite element (FE) modeling is utilized to simulate the local temperature evolution and crystallization for different combinations of parameters. This combined experimental/numerical approach will provide guidelines for the manufacturing of Fe-based BMGs with high density and high amorphous fractions, thus contributing to enhance their potential as enablers of energy efficient electric mobility solutions.

2. Experimental procedure

A commercial Kuamet 6B2 Fe-based alloy powder was used as feedstock material for the present study. The alloy, with composition $Fe_{73.7}B_{11}Si_{11}Cr_{2.3}C_2$ [at%], was produced by Epson ATMIX Japan by spinning water atomization (SWAP) [8]. The particle size distribution, which was evaluated with a Bettersize analyzer, was characterized by D_{10}, D_{50} and D_{90} values of 11, 30, and 61 μm, respectively. The powder density and flowability were measured following ASTM standards [44,45]. The apparent powder density was 4 g/cm^3, the tapped density amounted to 4.2 g/cm^3, and the powder did not flow continuously through the Hall flow meter. Nevertheless, the powder flow was excellent during LPBF trials and uniform layers were deposited through the entirety of the build jobs. A Perkin Elmer DSC8000 device was used for differential scanning calorimetry (DSC) evaluation of the amorphous fraction of the virgin powder. The latter was calculated as the ratio of the enthalpy of crystallization in the powder's heating curve and the enthalpy of crystallization of a fully amorphous Kuamet6B2 melt-spun ribbon ($\Delta H_{cr,sample}/\Delta H_{cr,ribbon}$), following a heating rate of 20 K/min.

The LPBF system used in this study was a Renishaw RenAM500Q Flex machine equipped with four 500 W Yb-fiber lasers, which was operated using pulsed wave emission. A reduced build volume (RBV) unit was utilized to limit the use of powder. A total of 28 prisms with dimensions 8x8x5.4 mm^3 were printed on 316 L steel substrates with different combinations of parameters, which are summarized in Table 1. The layer thickness (t) was maintained at 30 μm, i.e., equal to the D_{50} value of the feedstock powder, and the hatch distance (h) and the laser point distance (pd) were both set at 80 μm, which is the approximate size of the laser's spot diameter. LPBF processing was carried out using two values of laser power (P = 120 and 160 W) and two values of laser exposure time (t_{ON} = 80 and 120 μs). The corresponding scan speed values (v= 888 and 615 mm/s, respectively), which can be calculated as v = pd/(t_{ON} + 10 μs), are also reported in Table 1. For each P and v combination, one sample was printed using a conventional meander strategy with 67º rotation between layers and with the minimum default delay time (t_{OFF}) at the end of each scan track (1 ms) and six additional prisms were manufactured with t_{OFF} values of 50, 100, 150, 200, 250,

Table 1
LPBF processing parameters and normalized volumetric energy density.

Group	Sample ID	P (W)	t_{ON} (μs)	t_{OFF} (ms)	v (mm/s)	E^*
Group A	S1	160	120	1	615	7.08
	S2	160	120	50	615	5.61
	S3	160	120	100	615	5.59
	S4	160	120	150	615	5.59
	S5	160	120	200	615	5.58
	S6	160	120	250	615	5.58
	S7	160	120	300	615	5.58
Group B	S8	160	80	1	888	4.45
	S9	160	80	50	888	3.87
	S10	160	80	100	888	3.86
	S11	160	80	150	888	3.86
	S12	160	80	200	888	3.86
	S13	160	80	250	888	3.86
	S14	160	80	300	888	3.85
Group C	S15	120	120	1	615	4.97
	S16	120	120	50	615	4.20
	S17	120	120	100	615	4.19
	S18	120	120	150	615	4.19
	S19	120	120	200	615	4.19
	S20	120	120	250	615	4.18
	S21	120	120	300	615	4.18
Group D	S22	120	80	1	888	3.21
	S23	120	80	50	888	2.90
	S24	120	80	100	888	2.89
	S25	120	80	150	888	2.89
	S26	120	80	200	888	2.89
	S27	120	80	250	888	2.89
	S28	120	80	300	888	2.89

and 300 ms. The associated increases in build time for one single sample when introducing these delays are, respectively, 56 %, 116 %, 175 %, 234 %, 294 %, and 353 %. A schematic representation of this modified meander scanning strategy is displayed on Fig. 1, where areas with different degrees of heat accumulation are qualitatively depicted using a color code. As shown in Fig. 1, the introduction of time delays is aimed at reducing heat accumulation in the printed sample. The 28 LPBF-manufactured samples have been divided into 4 groups (A to D), each with common P and v values, and with different t_{OFF} times (A (160 W, 615 mm/s); B (160 W, 888 mm/s); C (120 W, 615 mm/s); D (120 W, 888 mm/s)). The normalized volumetric energy (E^{*}) corresponding to each of the 28 LPBF-manufacturing conditions, which is also shown in Table 1, was calculated as suggested by Thomas et al. [46] and Phan et al. [47] and its derivation is detailed in the Supplementary Material. In-operando infrared emission measurements were acquired with Renishaw's RenAM500Q built-in photodiode. The sensor is calibrated to record emissions of wavelengths between 1100 – 2000 nm, which are associated to the thermal emissions of the melt pool. Data post-processing was carried out using Renishaw's InfiniAM Spectral software and MATLAB.

The LPBF-manufactured samples were detached from the build platform using a Struers Secotom-20 disc cutting machine. Subsequently, each sample was cut in two halves along a plane parallel to the build direction (BD) for characterization purposes. One half was used to measure density, to analyze defects, and for (micro)structural examination. The second half was utilized for magnetic characterization followed by calorimetry tests. The density of each sample was measured by image analysis from optical micrographs. Optical microscopy (OM) was carried out using an Olympus BX51 light microscope and the software ImageJ/Fiji with the Trainable Weka Segmentation plug-in [48] was utilized to segment pores and cracks. Metallographic preparation for OM examination included grinding with sandpaper of grit sizes ranging from 300 to 2400 and polishing with diamond pastes of sizes decreasing from 9 μm to 1 μm, followed by chemical-polishing with a 0.04 μm colloidal silica suspension to achieve a mirror-like surface finish. The melt-pool geometry was examined in samples additionally etched using a 10:10:1 solution of 98 % ethanol, distilled water, and 65 % nitric acid. A 3x3x1 mm^3 piece was cut from each printed sample to evaluate the fraction of amorphous phase by DSC in a Perkin Elmer DSC8000 system using the same methodology as for the powders. Microtexture analyses were conducted using an Apreo 2S (ThermoFisher Scientific) field emission gun scanning electron microscope (FEGSEM) equipped with an Oxford Instruments electron backscattered diffraction (EBSD) detector, a CCD camera, and the Aztec data acquisition and analysis software package. EBSD maps of the crystalline regions were acquired using 20 kV, a current of 3.2 nA, a working distance of 13 mm, and a step size of 120 nm. Surface finishing for EBSD measurements was performed as explained above for OM sample preparation.

Hysteresis loops were measured at room temperature for all LPBF-manufactured samples using a LakeShore vibrating sample magnetometer (VSM) by applying a DC magnetic field in the range of ± 800 kA/m. The coercive field (H_c) was evaluated for each sample from the hysteresis loop after the subtraction of the sample holder's diamagnetic contribution.

3. Simulation

3.1. Thermo-metallurgical model

A thermo-metallurgical finite element method (FEM)-based simulation of the LPBF process is carried out to understand the effect of time delays on the (micro)structure of the Kuamet 6B2 manufactured samples. The thermal model is similar as described in [49]. The evolution of temperature in the LPBF-manufactured parts (domain) is computed by solving the heat transfer equation:

$$\rho c_p \frac{\partial T}{\partial t} = \nabla \bullet (k \nabla T) + Q_l + Q_\phi, \tag{1}$$

where ρ is the density, c_p is the specific heat capacity, k is the isotropic conductivity, T is the temperature, t is the time, Q_l is the absorbed heat due to the laser incidence, and Q_ϕ is the absorbed/released heat due to melting/solidification. The laser source contribution (Q_l) is computed as [50]:

$$Q_l = \alpha_p \frac{G_l I_z}{H_l}, \tag{2}$$

where α_p is the laser absorptivity, $G_l = \frac{2P}{\pi \varnothing^2} \exp\left(-2 \frac{(x-x_l)^2 + (y-y_l)^2}{\varnothing^2} \right)$ is the Gaussian distribution at the irradiated surface, $I_z = \frac{1}{0.75}\left[-2.25\left(\frac{z_l - z}{H_l}\right)^2 + 1.5\left(\frac{z_l - z}{H_l}\right) + 0.75 \right]$ is a parabolic decay along the laser penetration direction, H_l is the laser penetration depth, P is the laser power, $\varnothing$ is the diameter of the laser spot, and (x_l, y_l) are the coordinates of center of the laser spot that irradiates the surface located at z_l, referred to the Cartesian coordinate system (x, y, z). The contribution Q_ϕ in Eq. 1 is computed by taking into account the latent heat involved in melting/solidification as $Q_\phi = \rho L_f \frac{\partial f_s}{\partial t}$, where L_f is the latent heat of fusion and f_s is the solid volume fraction that is computed by the metallurgical model. The applied boundary conditions are given by Newton's law $q_c = -h_c(T - T_\infty)$, where q_c is the normal heat flux, h_c is the interfacial heat transfer coefficient, and T_∞ is the temperature of the environment.

Based on the temperature profile and history predicted from the thermal model described above, we apply a simple metallurgical model to qualitatively assess the formation of crystalline regions. Whenever a region is melted, i.e. when the local temperature exceeds the alloy liquidus temperature (T_L), we consider that the resulting default state from the fast cooling is fully amorphous, since the critical casting thickness is approximately 150 μm, i.e., around the width of a printed track, and the cooling rate of LPBF ($10^5 - 10^7$ K/s) [26] is substantially higher than that typical of casting processes ($10^0 - 10^2 K/s$) [51]. Hence, we assume that any crystalline region is purely the result of solid-state devitrification within a relevant temperature range, comprised between the liquidus and solidus (T_S) or final eutectic (T_E) temperatures. The temperature range for devitrification is calibrated to experimental data, and the residence time of the temperature within that range, τ, can be directly correlated to the extent and location of crystalline phases, as

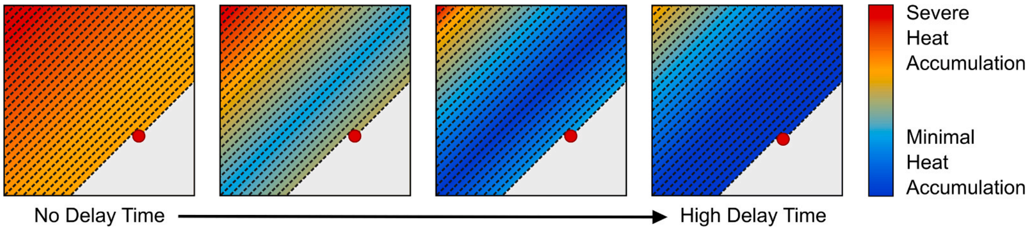

Fig. 1. Schematic representing the influence of time delays on heat accumulation.

shown later in Section 4.3 (Fig. 8).

The proposed model is implemented into the Abaqus finite element software by programming Fortran user subroutines, using the SoftGLASS plug-in [52]. The equations are solved on a discretized domain, which allows to compute the temperature and phase evolutions into the whole geometry.

3.2. Model parameters

The 3D simulations are performed in a domain consisting of a previously deposited bulk substrate. The thermal and material properties used to perform the simulations are summarized in Tables 2–4. α_p and $\boldsymbol{H_l}$ were calibrated to get a good match between the measured and simulated melt pool sizes. The material's thermal properties (c_p, L_f, T_S and T_L) were obtained through differential thermal analysis on a NETZSCH STA 449 Jupiter system. The c_p in the liquid phase is assumed equal to that of pure Fe at the melting temperature [53] due to the lack of data on the alloy under investigation. The values of c_p are summarized in Table 3. The thermal conductivity k is assumed equal to that of pure Fe due also to the lack of data [53]. The variation of k with temperature is summarized in Table 4.

3.3. Simulated LPBF processing conditions and validation

To elucidate the influence of time delays on crystallization, the thermo-metallurgical FEM-based model was utilized to simulate laser melting of a single track processed using P = 160 W and v = 615 mm/s (group A) and of double tracks manufactured with the same P and v, with a hatch distance of 80 µm, and with time delays (t_{OFF}) of 1, 50, and 300 ms (as in samples S1, S2, and S7). The laser spot size was taken as 80 µm.

The model validation campaign included laser melting of single and double tracks with the processing parameters utilized for the simulations and using the Renishaw RenAM500Q Flex system on top of a fully amorphous Kuamet 6B2 plate. The latter was produced by copper mold suction casting with a thickness of approximately 150 µm, which is close to the critical casting thickness for this alloy. The absence of crystalline phases in the substrate prior to laser melting was verified by synchrotron X-ray diffraction (XRD) at the Deutsches Elektronen-Synchrotron (DESY, Germany). The corresponding XRD pattern is illustrated in Supplementary Fig.2. It can be clearly seen that the sample presents a fully amorphous structure, characterized by two broad halos around 2θ = 45° and 80°. Before laser melting the amorphous plate was fixed to a 316 L steel substrate within the RBV using double-sided copper tape and the stage position was adjusted to place the top surface of the amorphous plate at the focal plane of the laser.

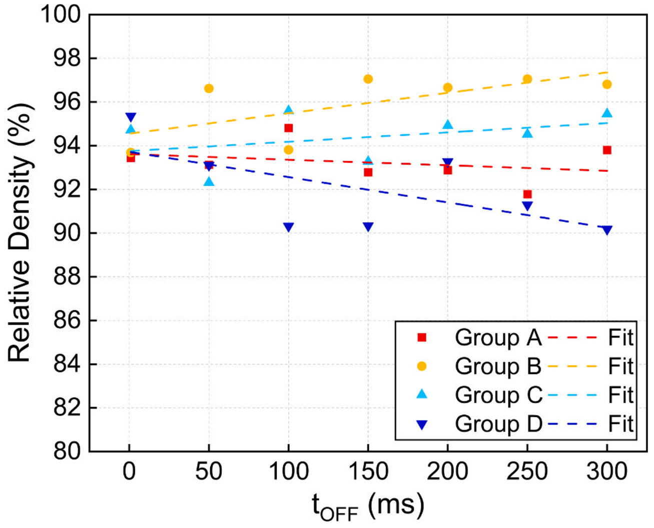

Fig. 3. Influence of the time delay on the density of the LPBF manufactured prisms. The dotted lines are first-degree exponential decay fits for groups A to D.

Cross sections of the single track and double track melt-pools perpendicular to the scan direction (SD) were prepared for EBSD examination. With that purpose, the substrate plate was held by pins and mounted in conductive resin with the lasered surface perpendicular to the bottom plane, such that the cross section of the melt pools generated by the melted tracks would be visible after grinding and polishing using the procedures described for EBSD sample preparation in Section 2.

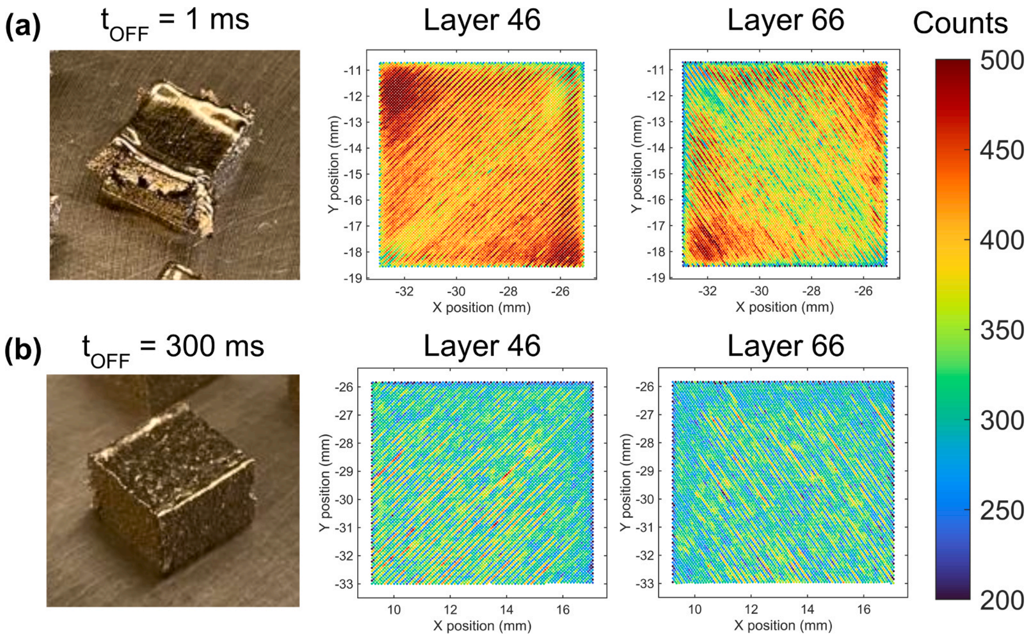

Fig. 2. Normalized infrared melt pool emission measured in-operando in the RenAM500Q LPBF system during processing of group A samples (a) S1 (P = 160 W, v = 615 mm/s, t_{OFF} = 1 ms) and (b) S7 (P = 160 W, v = 615 mm/s, t_{OFF} = 300 ms) at two representative layers (46 and 66).

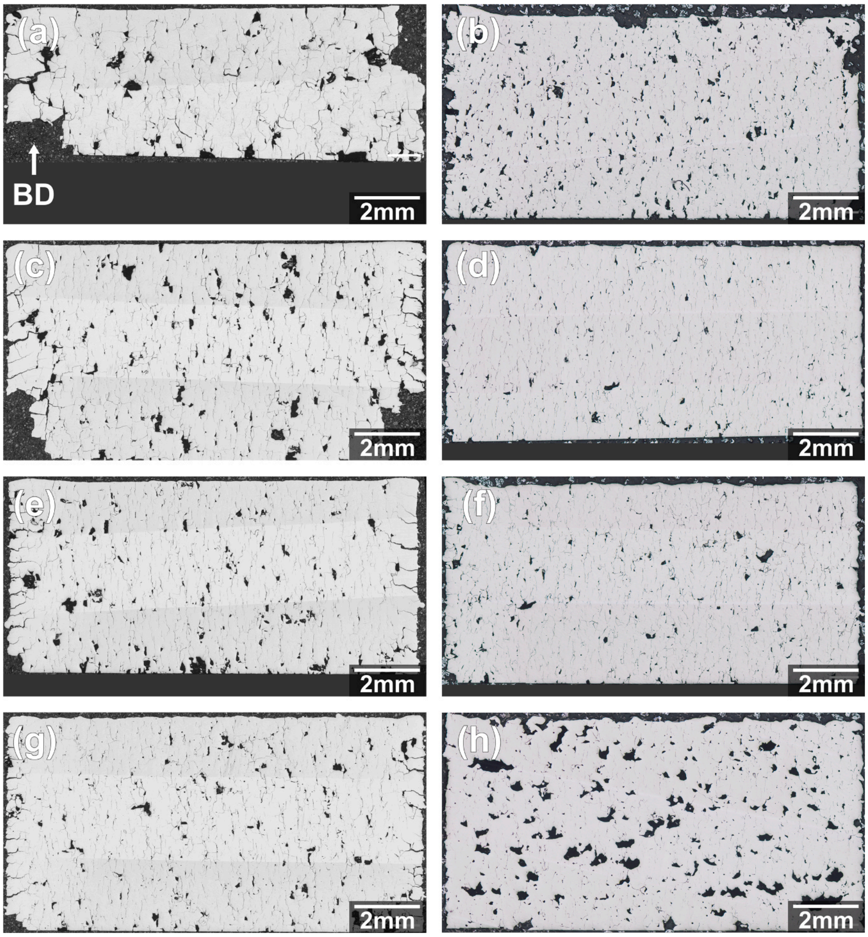

Fig. 4. Optical micrographs illustrating the defect structure in the following samples: (a) group A S1 (1 ms), (b) group A S7 (300 ms), (c) group B S8 (1 ms), (d) group B S14 (300 ms), (e) group C S15 (1 ms), (f) group C S21 (300 ms), (g) group D S22 (1 ms), (h) group D S28 (300 ms). The imaged cross-sections are parallel to BD.

4. Results

4.1. Influence of time delays on processability

All samples in groups A to D exhibited good dimensional stability, with the exception of sample S1 (group A), with the highest E^* (7.08), where severe warping and delamination effects were observed. However, as shown in Fig. 2, the introduction of time delays led to improved processability and excellent dimensional stability in group A samples. Fig. 2 illustrates the outer appearance of samples S1 (t_{OFF}=1 ms, which is the minimum default time delay, Fig. 2a) and S7 (t_{OFF}=300 ms, Fig. 2b). It can be clearly seen that, while sample S1 experienced severe warping effects, sample S7 retained its original shape. To elucidate the origin of the improved processability with the introduction of time delays, the infrared melt-pool emission during LPBF processing of samples S1 and S7 was measured in-operando using a spectrometer installed at the RenAM500Q system. Measurements were performed at two representative layers (46 and 66) where the direction of the scan tracks is oriented along the square cross section's diagonal. The results are shown in Fig. 2. In the absence of time delays (sample S1, Fig. 2a), significant heat accumulation is observed at the corners, where the scan path is very short. However, switching off the laser after each track for 300 ms (sample S7, Fig. 2b) enables sample cooling before the next track is melted, limiting heat accumulation, and hence homogenizing the temperature across the printed layer.

4.2. Influence of time delays on density and melt-pool geometry

Fig. 3 illustrates the influence of the time delay on the density for samples belonging to groups A, B, C, and D. All samples have a relative density above 90 %. Despite the evident scatter within each group, it can be concluded from Fig. 3 that group B and C samples, with intermediate E^* values (between 3.85 and 4.97), have on average the highest density, while group A and D samples, with E^* values above 5.58 and below 3.21, respectively, possess a higher fraction of porosity. In samples belonging to groups A, B, and C, the increase in t_{OFF} from 1 ms to 300 ms has a small and/or positive effect on the density. However, most notably, in samples belonging to group D, which have the lowest E^*, an increase in the time delay leads clearly to a notable decrease in density. Fig. 4 depicts several optical micrographs illustrating the defect structure in cross sections parallel to the build direction (BD) of two samples from each group (A to D) with, respectively, 1 and 300 ms delay. In agreement with Fig. 3, it can be seen that increasing the time delay in groups B and C samples (Figs. 4c,d and 4e,f, respectively) leads to a moderate increase in density. However, in group A samples (Fig. 4a,b) increasing the time delay does not eliminate excessive melting porosity, and in group D samples (Fig. 4g,h) time delays introduce a large fraction of lack of fusion defects. Cracks are present in all the manufactured samples, in agreement with earlier studies [31], and the crack area fraction (~2 %) appears to be fairly independent of the processing conditions.

Fig. 5 illustrates the influence of time delays on the geometry of the melt-pools belonging to all sample groups (A to D). In particular, the effect of the time delay on the melt-pool width (W) (Fig. 5a), depth (D)

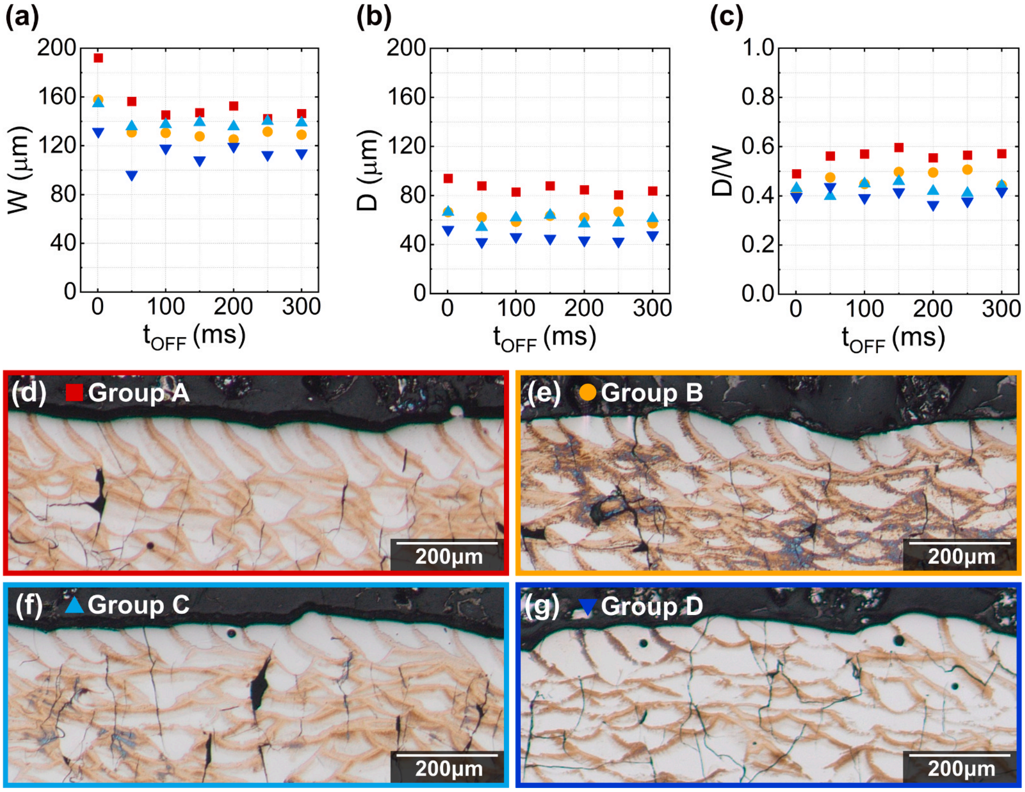

Fig. 5. Influence of the time delay on (a) the average melt pool width, (b) the average melt pool depth, and (c) the depth to width ratio for samples belonging to groups A to D; (d-g) optical micrographs of etched LPBF samples showing the morphology of melt pools at the top layer for samples manufactured with a time delay of 50 ms in groups (d) A (S2), (e) B (S9), (f) C (S16) and (g) D (S23).

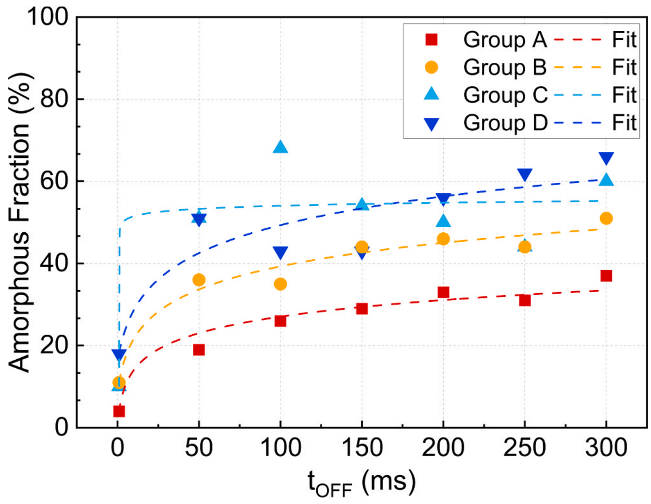

Fig. 6. Influence of time delay on the fraction of the amorphous phase measured by DSC. The dotted lines are logarithmic fits for groups A to D.

(Fig. 5b), and depth to width ratio (D/W) (Fig. 5c), measured at the top layer, is shown. Figs. 5a and 5b reveal that both W and D, but especially W, decrease for all sample groups when a time delay of 50 ms is introduced, and then both W and D remain fairly stable for higher time delays. As shown in Fig. 5c, the D/W ratio increases slightly with the time delay for groups A and B and it remains stable for groups C and D. For all samples, the D/W ratio ranges between 0.35 and 0.6, suggesting a transition melting mode, where both conduction and keyhole melting are present [54]. Indeed, a close look at the geometry of melt pools at the top layer of samples manufactured with a time delay of 50 ms in groups A (Fig. 5d), B (Fig. 5e), C (Fig. 5f), and D (Fig. 5g) reveals the presence of melt-pools with tear-drop shape, characteristic of keyhole mode melting, intermingled with others that resemble a half-moon, which are more typical of conduction melting.

4.3. Influence of time delays on the amorphous fraction

Fig. 6 illustrates the influence of time delays in the volume fraction of the amorphous phase (AM%) measured by DSC in all manufactured samples. The highest amorphous fractions, ranging between 60 % and 70 %, are obtained in groups C and D, while group A specimens exhibit the lowest AM% due to the excessive energy input. In general, the introduction of time delays leads to an increase in AM% in the LPBF manufactured prisms. The largest variation of AM% is observed for a time delay of 50 ms, and then the increase in AM% is smoother for larger delay times. In particular, the increase in AM% achieved when introducing a time delay of 50 ms in groups A to D amounts to + 15 %, + 25 %, + 41 %, and + 33 %, respectively. Also, the increase in AM% achieved when introducing a time delay of 300 ms in groups A to D amounts to + 33 %, + 40 %, + 50 %, and + 48 %, respectively.

In order to understand the effect of time delays in AM%, the thermo-metallurgical FEM-based model described in Section 3 is utilized to simulate laser melting of a single track processed using $P = 160$ W, $v = 615$ mm/s (i.e., with laser parameters equivalent to those of group A specimens) and of double tracks manufactured with the same P and v, with a hatch distance of 80 µm, and with t_{OFF} of 1, 50, and 300 ms (as in group A samples S1, S2, and S7). The map of Fig. 7a illustrates as an example the temperature distribution during one of the double track simulations. The node from where the temperature readings were captured is located 0.5 mm away from the edge of the simulated volume (Fig. 7a) at a location around the center of the melt pool of the first track, and within the heat affected zone (HAZ) of the second track, as indicated by the star symbol in Figs. 7b and 7c, respectively. Fig. 7d illustrates the

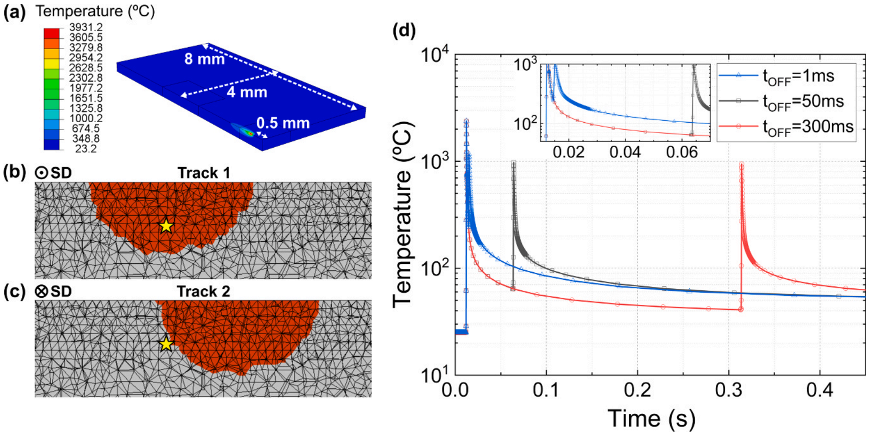

Fig. 7. (a) A representative image of the FEM-simulated temperature distribution during a double track simulation. (b,c) Cross sections of simulated melt pools perpendicular to the scan direction (SD) during the (b) first and (c) second tracks. The red semicircles indicate the liquid material during scanning and the yellow star marks the location of the node where temperature profiles were evaluated. (d) Simulated temperature evolution during double track experiments using group A conditions with $t_{OFF} = 1$, 50, and 300 ms. The temperature profiles correspond to a location 0.5 mm away from the edge of the simulated volume.

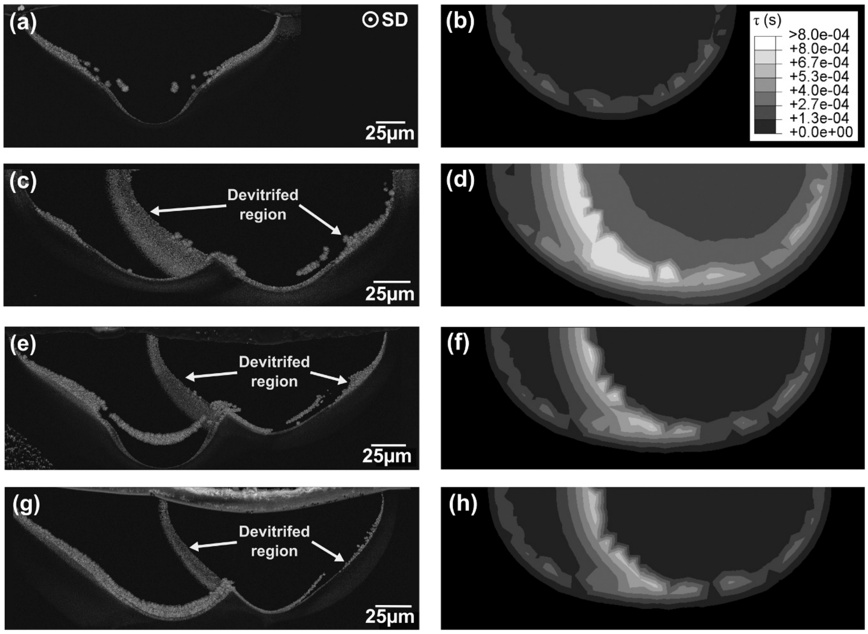

Fig. 8. (a,c,e,g) EBSD band contrast maps illustrating cross sections perpendicular to the scan direction of group A (a) single track and (c,e,g) double tracks with (c) $t_{OFF} = 1$ ms, (e) $t_{OFF} = 50$ ms, and (g) $t_{OFF} = 300$ ms; (b,d,f,h) FEM-simulated τ maps corresponding to (b) the single track, and (d,f,h) the double tracks with (d) $t_{OFF} = 1$ ms, (f) $t_{OFF} = 50$ ms (h) $t_{OFF} = 300$ ms.

Table 2
Thermal and material parameters used for simulations.

ρ Bulk material (kg/m^3)	α_p	H_l (μm)	h_c Top domain surface (W/m^2/°C)	h_c Bottom domain surface (W/m^2/°C)	L_f (J/kg)	T_∞ (°C)	T_S (°C)	T_L (°C)
7200	0.6	62	50 [49]	500 [49]	272000	25	1050	1150

Table 3
Specific heat capacity as a function of temperature.

T (°C)	$T \leq T_S$ (solid state)	$T \geq T_L$ (liquid state)
c_p (J/kg/°C)	527	761

temperature profiles corresponding to the simulated single and double tracks. While the first temperature peaks of all three conditions are identical, the maximum temperature of the second peak decreases from 1166 °C when $t_{OFF} = 1$ ms to 976 °C when $t_{OFF} = 50$ ms, and to 943 °C when $t_{OFF} = 300$ ms. Most importantly, the temperature at the selected location when the second track is printed (T_0) decreases from 242 °C when $t_{OFF} = 1$ ms to 64 °C when $t_{OFF} = 50$ ms, and to 41 °C when $t_{OFF} = 300$ ms.

Single and double tracks were laser melted over an amorphous Kuamet6B2 substrate with the same manufacturing conditions used in the simulations. Fig. 8 compares EBSD band contrast maps of cross sections perpendicular to the scan direction of the single track (Fig. 8a) and of the double tracks (Fig. 8c,e,g) with the corresponding FEM-

Table 4
Thermal conductivity of the bulk material as a function of temperature [53].

T (°C)	20	100	200	400	600	800	927	1050	1055	1500
k (W/m/°C)	73.3	68.2	61.5	48.6	38.9	29.7	29.7	34	33	33

simulated maps illustrating τ, the computed weighted time that the material remains at a temperature between T_X and T_S (equation 3, Section 3) (Fig. 8b,d,f,h). In the EBSD band contrast maps of Fig. 8a,c,e,g the gray areas correspond to crystalline regions while the black areas represent regions where the amorphous phase dominates. Comparison of experiments and simulations prove that there is a direct proportionality between the proposed weighted time, τ, and the crystalline volume fraction. Figs. 8a and 8b suggest, furthermore, that devitrification during laser melting of single tracks is comparatively limited, even when high E^* conditions (group A) are used. However, as shown in Figs. 8c and 8d, when a second track is melted adjacently with the minimum default delay time (1 ms) devitrification takes place within a significantly large region within the HAZ. The devitrified region has been pointed with arrows in Figs. 8c, 8e and 8g. Increasing the time delay to 50 (Fig. 8e,f) and 300 ms (Fig. 8 g,h) reduces progressively the size of the devitrified region in the overlap of the two tracks.

In summary, the increase in AM% with the introduction of time delays (Fig. 6) is driven by the reduction of T_0 in the amorphous regions solidified during the first pass (Fig. 7d), an effect that becomes more pronounced as the delay time increases. Consequently, during the second laser pass, the amorphous regions with lower T_0 within the HAZ spend less time at temperatures between T_X and T_S, leading to a lower degree of devitrification (Fig. 8e,f,g,h).

Fig. 9 illustrates several EBSD maps corresponding to the LPBF-manufactured Kuamet6B2 samples S2 (group A, E^* = 5.61, AM%= 19 %) (Figs. 9a-c) and S23 (group D, E^* = 2.90, AM%=55 %) (Fig. 9b,d). In the band contrast maps of Figs. 9a and 9b the crystalline regions are depicted in gray and the amorphous regions are colored in black. The step size used to measure these maps was 120 nm and thus the presence of smaller nanocrystals within the amorphous regions cannot be ruled out. Most importantly, Figs. 9a and 9b evidence that, in both specimens, crystallization takes place along the melt pool boundaries and that higher E^* values result in wider crystalline regions, in agreement with Fig. 6. The inverse pole figure maps of Figs. 9c and 9d, which illustrate the orientation of the build direction (BD), reveal that, irrespective of E^*, crystallites do not have any preferred orientation and are endowed with a relatively equiaxed shape. The grain size is, in both cases, below 4 μm, with the largest grains located close to the melt-pool boundary and a gradient of decreasing sizes with increasing distance from the melt-pool. The dominant phase is Fe_3Si, in agreement with earlier studies [31].

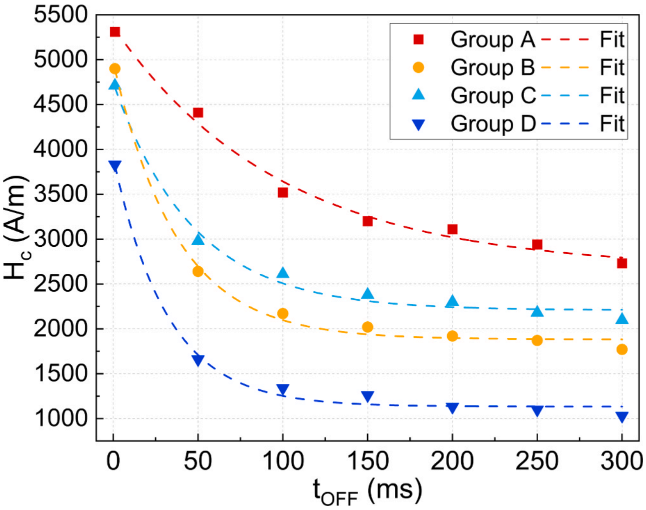

Fig. 10. Effect of the introduction of time delays on the coercive field of the LPBF-manufactured Kuamet6B2 prisms. The dashed lines are exponential decay fits corresponding to samples from groups A to D.

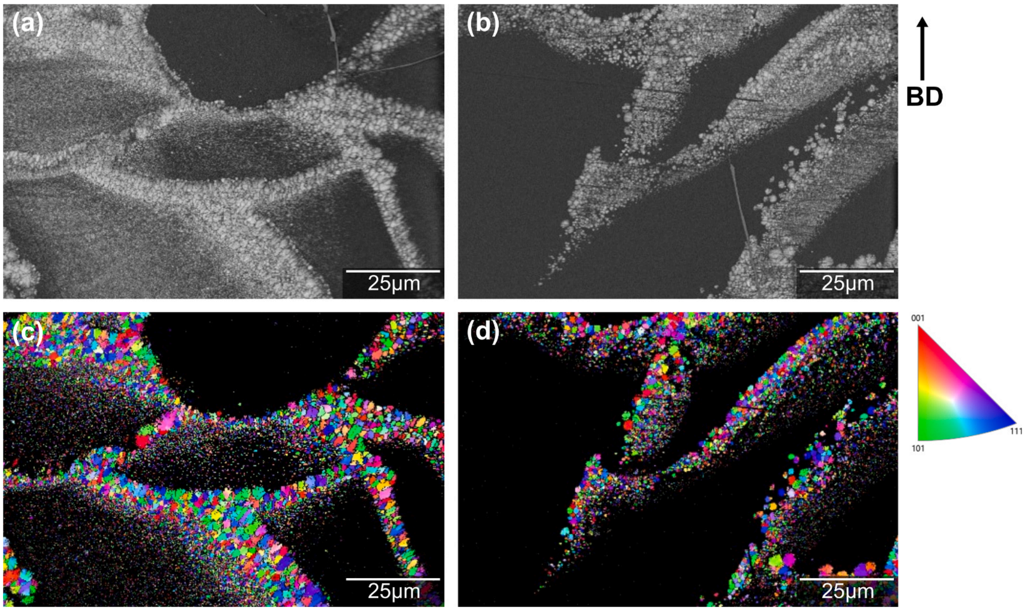

Fig. 9. EBSD maps of two LPBF processed Kuamet6B2 specimens processed with a time delay of 50 ms and two extreme E^* values: (a and c) sample S2 (group A, E^* = 5.61, AM%=19 %) and (b and d) sample S23 (group D, E^* = 2.90, AM%=55 %). (a, b) Band contrast maps showing in gray the crystalline regions and in black the amorphous regions, where the presence of nano-crystals smaller than the EBSD detection limit cannot be ruled out; (c, d) inverse pole figure maps illustrating the orientation of the build direction.

4.4. Influence of time delays on the coercivity

Fig. 10 illustrates the evolution of the coercive field (H_c) with the time delay for LPBF-manufactured Kuamet6B2 specimens belonging to groups A to D. In general, the introduction of time delays leads to a decrease in H_c in the LPBF manufactured prisms. The largest variation of H_c is observed for a time delay of 50 ms, and for larger time delays the coercivity decreases more smoothly, tending towards a stable value. In particular, the reduction in H_c achieved when introducing a time delay of 50 ms in groups A to D amounts to −900 A/m (-16.9 %), −2260 A/m (-46.1 %), −1730 A/m (-36.7 %), and −2170 A/m (-56.7 %), respectively. The total reduction in H_c achieved when introducing a time delay of 300 ms in groups A to D amounts to −2580 A/m (-48.6 %), −3130 A/m (-63.9 %), −2610 A/m (-55.4 %), and −2800 A/m (-73.1 %), respectively. The lowest H_c values, approaching 1000 A/m, are obtained in D specimens, which were processed with the lowest energy input.

5. Discussion

5.1. Time delays as a tool to overcome the density-amorphous fraction paradox

Previous works on LPBF of Fe-based metallic glasses, which are endowed with very low GFA, have reported an inverse relationship between the relative part density and the amorphous fraction of printed parts [26–36,55]. High energy LPBF conditions reportedly give rise to high density but low amorphous fractions, and low energy LPBF conditions result in higher amorphous fractions but introduce lack of fusion defects. Since soft magnetic applications require dense and highly amorphous components, this “density-amorphous fraction paradox” poses critical challenges to the fabrication of Fe-based components by LPBF.

Significant efforts have been made in the BMG community to overcome this processability issue. For instance, Nam et al. [33] used an LPBF remelting strategy on Kuamet6B2 to first consolidate the powder into a solid layer that was subsequently remelted. This approach yielded samples with relative densities of up to 96 % and amorphous fractions of 47 %. Zrodowski et al. [56] also implemented an LPBF double scanning strategy on Kuamet 6B2, where remelting was performed following a so-called “point-random” sequence, in which consecutive exposure points are chosen randomly at distances larger than 1 mm within the sample to avoid heat accumulation. Reportedly, such separation gives a longer time for exposed areas to cool down before an adjacent region is melted, hence minimizing devitrification. While this approach yielded samples with simultaneously high densities (94 %) and high AM% (90 %), the use of double scanning leads to very long manufacturing times, and the point-random strategy is not feasible in most commercial LPBF manufacturing systems. Additionally, this strategy presents reproducibility challenges when manufacturing complex-geometry parts.

In this work, a conventional meander scan strategy, with 67° interlayer rotations, which can be easily replicated in most LPBF systems, has been modified by the introduction of time delays at the end of each scan track. Fig. 11 illustrates the variation of the density with respect to AM% for all the Kuamet 6B2 samples manufactured within the present study. It can be seen that the use of time delays allows to improve the amorphous fraction while retaining high density values in samples within groups A, B, and C. In group D samples, which were processed with the lowest normalized volumetric energy density, an increase in AM% of 50 % is accompanied by a decrease in density of ~5.5 % due to the increase in lack of fusion defects with the introduction of time delays. Even in these samples, however, the decrease in density is comparatively much smaller than that observed in earlier studies for smaller increases in AM% [31].

In summary, this study demonstrates, for the first time, that a decoupling of the variations of the density and of the amorphous fraction can be achieved in Fe-based metallic glasses using a simple scanning strategy and varying only one single processing parameter (t_{OFF}). The introduction of time delays can be put forward as an effective tool to break the density/amorphous fraction paradox in these materials.

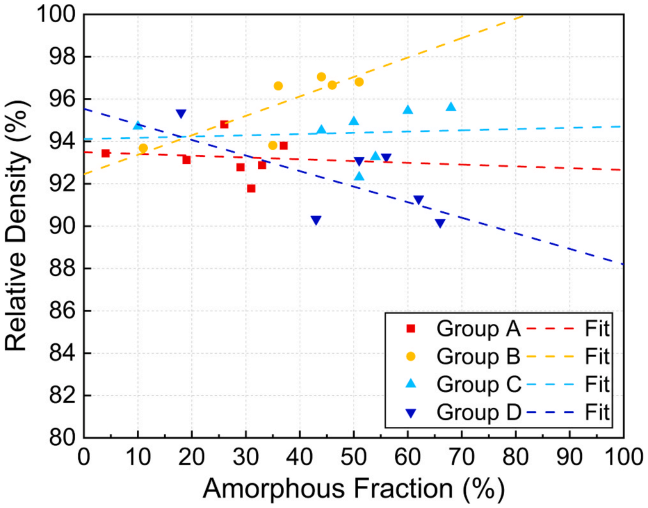

Fig. 11. Variation of the density with the fraction of the amorphous phase in LPBF manufactured Kuamet 6B2 samples belonging to groups A to D.

5.2. Understanding the relationship between the fraction of amorphous phase and H_c

In soft magnetic Fe-based alloys, coercivity is closely dependent on the amorphous fraction, grain size, and alloy composition. A higher amorphous fraction minimizes domain wall pinning by reducing grain boundaries, while nanocrystalline structures with grain sizes below 10 nm further lower coercivity due to reduced magnetocrystalline anisotropy and enhanced magnetic coupling through the amorphous matrix [57]. Additionally, compositional tuning, such as the inclusion of elements like Sn or B, can improve magnetic properties by optimizing internal stresses and magnetoelastic anisotropy [57].

Coercivity does not always decrease with an increasing amorphous fraction in Fe-based soft magnetic alloys due to the complex interplay of magnetoelastic anisotropy, internal stresses, and structural defects inherent in the amorphous matrix. While a fully amorphous structure eliminates grain boundaries that typically act as domain wall pinning centers, it introduces other sources of anisotropy, such as stress-induced magnetoelastic effects, which can hinder domain wall motion. Additionally, the absence of magnetic coupling between nanocrystals (as described by the Random Anisotropy Model) in a fully amorphous state prevents the averaging out of magnetocrystalline anisotropy, which is key to achieving ultra-low coercivity in nanocrystalline systems [58].

Fig. 12 shows the variation of the coercive field with respect to AM% in the Kuamet 6B2 LPBF-manufactured specimens belonging to groups A to D. The data corresponding to a SWAP-atomized powder and to a melt-spun ribbon of the same composition are plotted as a reference. In general, an inverse linear dependency between H_c and AM%, with a slope of −71 A/m, is observed when AM% $\leq$ 45 %, in agreement with earlier studies [31]. This AM% range includes all samples within groups A and B and the samples processed with 1 and 50 ms time delay from groups C and D. For processing conditions where AM% > 45 %, however, H_c becomes less dependent on AM%. This AM% range includes samples from groups C and D with time delays higher than 50 ms. In these samples, increases in AM% from ~50 to ~70 % lead only to comparatively minor variations of H_c. Additionally, samples from group D are characterized by coercivity values stabilizing around 1 kA/m. This behavior may arise from multiple factors that are beyond the scope of the present work. Notably, all samples still exhibit a relatively high

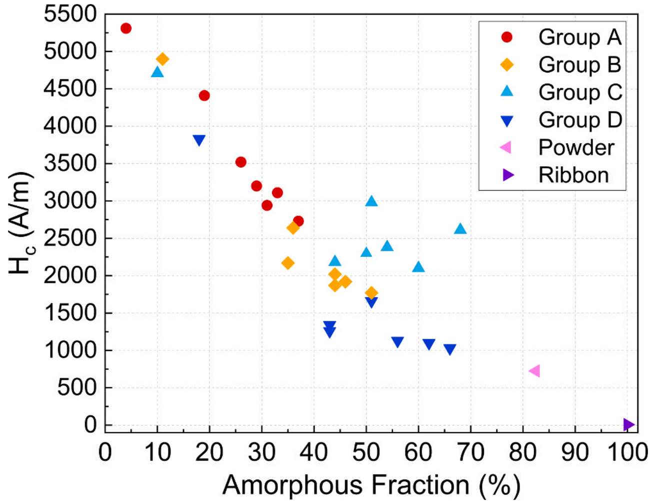

Fig. 12. Variation of the coercive field with respect to the amorphous fraction in the Kuamet 6B2 LPBF-manufactured specimens. The data corresponding to a SWAP-atomized powder and a melt-spun ribbon of the same composition are plotted as a reference.

crystalline fraction (not less than 30 %), mostly dominated by the Fe_3Si phase as shown in earlier studies [31], and which may also contain a minor presence of boride phases such as FeB, Fe_2B, and Fe_3B. These phases are known to significantly influence the magnetic properties of Fe-based soft magnetic alloys by increasing coercivity and reducing permeability [58], which likely accounts for the absence of further coercivity reduction beyond the observed plateau at 1 kA/m.

6. Conclusions

The aim of this study is to investigate the impact of introducing time delays (laser switch-off times) after each scan track of an LPBF meander scanning strategy on the processability, density, crystallinity, and coercive field (H_c) of Fe-based Kuamet 6B2 specimens. With that goal, LPBF is performed using two laser power levels (120 W and 160 W), two scan speeds (615 mm/s and 888 mm/s), and time delays ranging from 50 to 300 ms. Multiphysics FEM simulations are utilized to rationalize the influence of time delays on the temperature evolution and on crystallization during LPBF. The following conclusions can be drawn from this work:

1. Introducing time delays improves processability and dimensional accuracy in the samples manufactured with the highest normalized energy density (group A, with $P = 160$ W and $v = 615$ mm/s), reducing warping and delamination effects.
2. Glass/crystalline composites were obtained for all investigated LPBF conditions. The addition of time delays increases the amorphous fraction in the LPBF manufactured samples without compromising density. The most pronounced increases in the amorphous fraction are observed for time delays as short as 50 ms.
3. The introduction of time delays results in a lower T_0 in the solidified amorphous regions which, in turn, experience a lower degree of devitrification during subsequent laser passes. Although increasing time delays lead to progressively lower degrees of devitrification, the most pronounced change in the fraction of devitrified material occurs for time delays as short as 50 ms.
4. A strong inverse linear dependency exists between H_c and the amorphous fraction when the latter is smaller than 45 %; for higher fractions the dependency is significantly less pronounced.
5. The introduction of time delays is presented as a strategy with high potential to resolve the "density/amorphous fraction" paradox in Fe-based MGs, providing guidelines for LPBF manufacturing of these alloys for soft magnetic applications.

CRediT authorship contribution statement

M. Rodríguez-Sánchez: Conceptualization, Formal analysis, Investigation, Methodology, Visualization, Writing – original draft. **A.D. Boccardo:** Conceptualization, Methodology, Software, Writing – review & editing. **S. Sadanand:** Investigation, Methodology. **A. Ghavimi:** Formal analysis, Investigation, Methodology, Writing – review & editing. **R. Busch:** Funding acquisition, Project administration, Supervision, Writing – review & editing. **P. Sharangi:** Formal analysis, Investigation, Methodology, Writing – review & editing. **E. Ferrara:** Methodology, Validation. **G. Barrera:** Methodology, Validation. **P. Tiberto:** Funding acquisition, Resources, Supervision, Validation, Writing – review & editing. **D. Tourret:** Supervision, Validation, Writing – review & editing. **I. Gallino:** Funding acquisition, Project administration, Supervision. **M. T. Pérez-Prado:** Conceptualization, Funding acquisition, Resources, Supervision, Writing – review & editing.

Declaration of Competing Interest

The authors declare the following financial interests/personal relationships which may be considered as potential competing interests: Marcos Rodriguez Sanchez has patent #EP24383248.2 pending to Fundación IMDEA Materiales. If there are other authors, they declare that they have no known competing financial interests or personal relationships that could have appeared to influence the work reported in this paper.

Acknowledgments

This work has been carried out under the scope AM2SoftMag project, funded by the European Innovation Council through the HORIZON-EIC-2021-PATHFINDEROPEN-01 grant (GA: 101046870). The authors thank the rest of the AM2SoftMag partners for their involvement in the project. Extended acknowledgement is given to Teresa Nieto Valeiras for her assistance with LPBF trials.

Appendix A. Supporting information

Supplementary data associated with this article can be found in the online version at doi:10.1016/j.addma.2025.104922.

Data availability

Data will be made available on request.

References

[1] W. Klement, R.H. Willens, P. Duwez, Non-crystalline structure in solidified Gold–Silicon alloys, Nature 187 (1960) 869–870, https://doi.org/10.1038/187869b0.
[2] H.X. Li, Z.C. Lu, S.L. Wang, Y. Wu, Z.P. Lu, Fe-based bulk metallic glasses: glass formation, fabrication, properties and applications, Prog. Mater. Sci. 103 (2019) 235–318, https://doi.org/10.1016/j.pmatsci.2019.01.003.
[3] J.M. Silveyra, E. Ferrara, D.L. Huber, T.C. Monson, Soft magnetic materials for a sustainable and electrified world, Science 362 (2018) eaao0195, https://doi.org/10.1126/science.aao0195.
[4] J. Liu, F. Kong, C. Cheng, S. Yue, W. Song, H. Wang, A. Wang, Attractive magnetic properties in as-cast bulk metallic glasses, J. NonCrys. Solids 653 (2025) 123437, https://doi.org/10.1016/j.jnoncrysol.2025.123437.
[5] J. Shen, Q. Chen, J. Sun, H. Fan, G. Wang, Exceptionally high glass-forming ability of an FeCoCrMoCBY alloy, Appl. Phys. Lett. 86 (2005) 151907, https://doi.org/10.1063/1.1897426.
[6] M.G. Özden, N.A. Morley, Laser additive manufacturing of Fe-Based magnetic amorphous alloys, Magnetochemistry 7 (2021) 20, https://doi.org/10.3390/magnetochemistry7020020.
[7] H. Liebermann, C. Graham, Production of amorphous alloy ribbons and effects of apparatus parameters on ribbon dimensions, IEEE Trans. Magn. 12 (1976) 921–923, https://doi.org/10.1109/TMAG.1976.1059201.

[8] I. Otsuka, K. Wada, Y. Maeta, T. Kadomura, M. Yagi, Magnetic properties of Fe-based amorphous powders with high-saturation induction produced by spinning water atomization process (SWAP), IEEE Trans. Magn. 44 (2008) 3891–3894, https://doi.org/10.1109/TMAG.2008.2002249.

[9] Q. Halim, N.A.N. Mohamed, M.R.M. Rejab, W.N.W.A. Naim, Q. Ma, Metallic glass properties, processing method and development perspective: a review, Int. J. Adv. Manuf. Technol. 112 (2021) 1231–1258, https://doi.org/10.1007/s00170-020-06515-z.

[10] N. Sohrabi, J. Jhabvala, R.E. Logé, Additive manufacturing of bulk metallic glasses—process, challenges and properties: a review, Metals 11 (2021) 1279, https://doi.org/10.3390/met11081279.

[11] P. Zhang, J. Tan, Y. Tian, H. Yan, Z. Yu, Research progress on selective laser melting (SLM) of bulk metallic glasses (BMGs): a review, Int. J. Adv. Manuf. Technol. 118 (2021) 2017–2057, https://doi.org/10.1007/s00170-021-07990-8.

[12] C. Zhang, D. Ouyang, S. Pauly, L. Liu, 3D printing of bulk metallic glasses, Mater. Sci. Eng. R. Rep. 145 (2021) 100625, https://doi.org/10.1016/j.mser.2021.100625.

[13] H.R. Lashgari, M. Ferry, S. Li, Additive manufacturing of bulk metallic glasses: fundamental principle, current/future developments and applications, J. Mater. Sci. Technol. 119 (2022) 131–149, https://doi.org/10.1016/j.jmst.2021.09.068.

[14] C. Klein, C. May, M. Nienhaus, Magnetic performance of eddy current suppressing structures in additive manufacturing, Actuators 13 (2024) 94, https://doi.org/10.3390/act13030094.

[15] A. Plotkowski, J. Pries, F. List, P. Nandwana, B. Stump, K. Carver, R.R. Dehoff, Influence of scan pattern and geometry on the microstructure and soft-magnetic performance of additively manufactured Fe-Si, Addit. Manuf. 29 (2019) 100781, https://doi.org/10.1016/j.addma.2019.100781.

[16] Z. Yang, M. Markl, C. Körner, Predictive simulation of bulk metallic glass crystallization during laser powder bed fusion, Addit. Manuf. 59 (2022) 103121, https://doi.org/10.1016/j.addma.2022.103121.

[17] B. Li, V. Yakubov, K. Nomoto, S.P. Ringer, B. Gludovatz, X. Li, J.J. Kruzic, Superior mechanical properties of a Zr-based bulk metallic glass via laser powder bed fusion process control, Acta Mater. 266 (2024) 119685, https://doi.org/10.1016/j.actamat.2024.119685.

[18] J.J. Marattukalam, V. Pacheco, D. Karlsson, L. Riekehr, J. Lindwall, F. Forsberg, U. Jansson, M. Sahlberg, B. Hjörvarsson, Development of process parameters for selective laser melting of a Zr-based bulk metallic glass, Addit. Manuf. 33 (2020) 101124, https://doi.org/10.1016/j.addma.2020.101124.

[19] S. Hadibeik, H. Ghasemi-Tabasi, A. Burn, S. Lani, F. Spieckermann, J. Eckert, Controlling the glassy state toward structural and mechanical enhancement: additive manufacturing of bulk metallic glass using advanced laser beam shaping technology, Adv. Funct. Mater. 34 (2024) 2311118, https://doi.org/10.1002/adfm.202311118.

[20] X.P. Li, M.P. Roberts, S. O'Keeffe, T.B. Sercombe, Selective laser melting of Zr-based bulk metallic glasses: processing, microstructure and mechanical properties, Mater. Des. 112 (2016) 217–226, https://doi.org/10.1016/j.matdes.2016.09.071.

[21] S. Pauly, C. Schricker, S. Scudino, L. Deng, U. Kühn, Processing a glass-forming Zr-based alloy by selective laser melting, Mater. Des. 135 (2017) 133–141, https://doi.org/10.1016/j.matdes.2017.08.070.

[22] J. Wagner, M. Frey, M. Piechotta, N. Neuber, B. Adam, S. Platt, L. Ruschel, S. S. Riegler, H.R. Jiang, G. Witt, R. Busch, S. Kleszczynski, Influence of powder characteristics on the structural and mechanical properties of additively manufactured Zr-based bulk metallic glass, Mater. Des. 209 (2021) 109976, https://doi.org/10.1016/j.matdes.2021.109976.

[23] L. Deng, S. Wang, P. Wang, U. Kühn, S. Pauly, Selective laser melting of a Ti-based bulk metallic glass, Mater. Lett. 212 (2018) 346–349, https://doi.org/10.1016/j.matlet.2017.10.130.

[24] M. Frey, J. Wegner, E.S. Barreto, L. Ruschel, N. Neuber, B. Adam, S.S. Riegler, H. R. Jiang, G. Witt, N. Ellendt, V. Uhlenwinkel, S. Kleszczynski, R. Busch, Laser powder bed fusion of Cu-Ti-Zr-Ni bulk metallic glasses in the Vit101 alloy system, Addit. Manuf. 66 (2023) 103467, https://doi.org/10.1016/j.addma.2023.103467.

[25] M. Frey, J. Wegner, L. Ruschel, E.S. Barreto, S.S. Riegler, B. Adam, N. Ellendt, S. Kleszczynski, R. Busch, Additive manufacturing of Ni62Nb38 metallic glass via laser powder bed fusion, Prog. Addit. Manuf. (2025), https://doi.org/10.1007/s40964-025-01007-6.

[26] D. Ouyang, W. Xing, N. Li, Y. Li, L. Liu, Structural evolutions in 3D-printed Fe-based metallic glass fabricated by selective laser melting, Addit. Manuf. 23 (2018) 246–252, https://doi.org/10.1016/j.addma.2018.08.020.

[27] S. Gao, X. Yan, C. Chang, E. Aubry, P. He, M. Liu, H. Liao, N. Fenineche, Microstructure and magnetic properties of FeSiBCrC soft magnetic alloy manufactured by selective laser melting, Mater. Lett. 290 (2021) 129469, https://doi.org/10.1016/j.matlet.2021.129469.

[28] Q. Jiang, P. Zhang, J. Tan, Z. Yu, Y. Tian, S. Ma, D. Wu, Influence of the microstructure on mechanical properties of SLM additive manufacturing Fe-based bulk metallic glasses, J. Alloy. Compd. 894 (2022) 162525, https://doi.org/10.1016/j.jallcom.2021.162525.

[29] L. Thorsson, M. Unosson, M.T. Pérez-Prado, X. Jin, P. Tiberto, G. Barrera, B. Adam, N. Neuber, A. Ghavimi, M. Frey, R. Busch, I. Gallino, Selective laser melting of a Fe-Si-Cr-B-C-based complex-shaped amorphous soft-magnetic electric motor rotor with record dimensions, Mater. Des. 215 (2022) 110483, https://doi.org/10.1016/j.matdes.2022.110483.

[30] M.G. Özden, N.A. Morley, Optimizing laser additive manufacturing process for Fe-based nano-crystalline magnetic materials, J. Alloy. Compd. 960 (2023) 170644, https://doi.org/10.1016/j.jallcom.2023.170644.

[31] M. Rodríguez-Sánchez, S. Sadanand, A. Ghavimi, R. Busch, P. Tiberto, E. Ferrara, G. Barrera, L. Thorsson, H.J. Wachter, I. Gallino, M.T. Pérez-Prado, Relating laser powder bed fusion process parameters to (micro)structure and to soft magnetic behaviour in a Fe-based bulk metallic glass, Materialia 35 (2024) 102111, https://doi.org/10.1016/j.mtla.2024.102111.

[32] N. Luo, C. Scheitler, N. Ciftci, F. Galgon, Z. Fu, V. Uhlenwinkel, M. Schmidt, C. Körner, Preparation of Fe-Co-B-Si-Nb bulk metallic glasses by laser powder bed fusion: microstructure and properties, Mater. Charact. 162 (2020) 110206, https://doi.org/10.1016/j.matchar.2020.110206.

[33] Y.G. Nam, B. Koo, M.S. Chang, S. Yang, J. Yu, Y.H. Park, J.W. Jeong, Selective laser melting vitrification of amorphous soft magnetic alloys with help of double-scanning-induced compositional homogeneity, Mater. Lett. 261 (2020) 127068, https://doi.org/10.1016/j.matlet.2019.127068.

[34] S. Sadanand, M. Rodríguez-Sánchez, A. Ghavimi, R. Busch, P. Sharangi, P. Tiberto, E. Ferrara, G. Barrera, L. Thorsson, H.J. Wachter, I. Gallino, M.T. Pérez-Prado, Laser powder bed fusion of a Finemet-based alloy for soft magnetic applications, J. Laser Appl. 36 (2024) 042029, https://doi.org/10.2351/7.0001391.

[35] H.Y. Jung, S.J. Choi, K.G. Prashanth, M. Stoica, S. Scudino, S. Yi, U. Kühn, D. H. Kim, K.B. Kim, J. Eckert, Fabrication of Fe-based bulk metallic glass by selective laser melting: a parameter study, Mater. Des. 86 (2015) 703–708, https://doi.org/10.1016/j.matdes.2015.07.145.

[36] X.D. Nong, X.L. Zhou, Y.X. Ren, Fabrication and characterization of Fe-based metallic glasses by selective laser melting, Opt. Laser Technol. 109 (2019) 20–26, https://doi.org/10.1016/j.optlastec.2018.07.059.

[37] N. Sohrabi, T. Ivas, J. Jhabvala, J.E.K. Schawe, J.F. Löffler, H. Ghasemi-Tabasi, R. E. Logé, Quantitative prediction of crystallization in laser powder bed fusion of a Zr-based bulk metallic glass with high oxygen content, Mater. Des. 239 (2024) 112744, https://doi.org/10.1016/j.matdes.2024.112744.

[38] P.A. Hooper, Melt pool temperature and cooling rates in laser powder bed fusion, Addit. Manuf. 22 (2018) 548–559, https://doi.org/10.1016/j.addma.2018.05.032.

[39] B. Zheng, Y. Zhou, J.E. Smugeresky, E.J. Lavernia, Processing and behavior of Fe-based metallic glass components via laser-engineered net shaping, Metall. Mater. Trans. A 40 (2009) 1235–1245, https://doi.org/10.1007/s11661-009-9828-y.

[40] V.K. Balla, A. Bandyopadhyay, Laser processing of Fe-based bulk amorphous alloy, Surf. Coat. Technol. 205 (2010) 2661–2667, https://doi.org/10.1016/j.surfcoat.2010.10.029.

[41] X. Ye, Y.C. Shin, Synthesis and characterization of Fe-based amorphous composite by laser direct deposition, Surf. Coat. Technol. 239 (2014) 34–40, https://doi.org/10.1016/j.surfcoat.2013.11.013.

[42] A. Olleak, E. Adcock, S. Hinnebusch, F. Dugast, A.D. Rollett, A.C. To, Understanding the role of geometry and interlayer cooling time on microstructure variations in LPBF Ti6Al4V, Addit. Manuf. Lett. 9 (2024) 100197, https://doi.org/10.1016/j.addlet.2024.100197.

[43] K. Ettaieb, K. Godineau, S. Lavernhe, C. Tournier, Offline laser power modulation in LPBF additive manufacturing including kinematic and technological constraints, Rapid Prototyp. J. 29 (2022) 80–91, https://doi.org/10.1108/RPJ-02-2022-0062.

[44] ASTM B527-20, ASTM B527-20 standard test method for tap density of metal powders and compounds, ASTM Int, 2020.

[45] ASTM international, standard test methods for flow rate of metal powders using the hall flowmeter funnel, ASTM Stand, 2016.

[46] M. Thomas, G.J. Baxter, I. Todd, Normalised model-based processing diagrams for additive layer manufacture of engineering alloys, Acta Mater. 108 (2016) 26–35, https://doi.org/10.1016/j.actamat.2016.02.025.

[47] M.A.L. Phan, O. Dew, I. Todd, Predictive process diagram for parameters selection in laser powder bed fusion to achieve high-density and low-cracking built parts, Addit. Manuf. 85 (2024) 104145, https://doi.org/10.1016/j.addma.2024.104145.

[48] I. Arganda-Carreras, V. Kaynig, C. Rueden, K.W. Eliceiri, J. Schindelin, A. Cardona, H.S. Seung, Trainable weka segmentation: a machine learning tool for microscopy pixel classification, Bioinform 33 (2017) 2424–2426, https://doi.org/10.1093/bioinformatics/btx180.

[49] D. Tourret, R. Tavakoli, A.D. Boccardo, A.K. Boukellal, M. Li, J. Molina-Aldareguia, Emergence of rapid solidification microstructure in additive manufacturing of a magnesium alloy, Model. Simul. Mater. Sci. Eng. 32 (2024) 055012, https://doi.org/10.1088/1361-651X/ad4576.

[50] S. Price, B. Cheng, J. Lydon, K. Cooper, K. Chou, On process temperature in Powder-Bed electron beam additive manufacturing: model development and validation, J. Manuf. Sci. Eng. 136 (2014) 061019, https://doi.org/10.1115/1.4028485.

[51] T. DebRoy, H.L. Wei, J.S. Zuback, T. Mukherjee, J.W. Elmer, J.O. Milewski, A. M. Beese, A. Wilson-Heid, A. De, W. Zhang, Additive manufacturing of metallic components – process, structure and properties, Prog. Mater. Sci. 92 (2018) 112–224, https://doi.org/10.1016/j.pmatsci.2017.10.001.

[52] Patent pending. Application number: EP24383248.2.

[53] E.A. Brandes, G.B. Brook. Smithells Metals Reference Book, seventh ed, Elsevier Inc, 2013.

[54] J.P. Oliveira, A.D. LaLonde, J. Ma, Processing parameters in laser powder bed fusion metal additive manufacturing, Mater. Des. 193 (2020) 108762, https://doi.org/10.1016/j.matdes.2020.108762.

[55] L. Wang, H. Wang, Y. Liu, Z. Fu, T. Peng, J. Shen, S. Zhou, M. Yan, G. Wang, Y. Dai, Selective laser melting helps fabricate record-large bulk metallic glass: experiments, simulation and demonstrative part, J. Alloy. Compd. 808 (2019) 151731, https://doi.org/10.1016/j.jallcom.2019.151731.

[56] Ł. Żrodowski, B. Wysocki, R. Wróblewski, A. Krawczyńska, B. Adamczyk-Cieślak, J. Zdunek, P. Błyskun, J. Ferenc, M. Leonowicz, W. Święszkowski, New approach to amorphization of alloys with low glass forming ability via selective laser melting,

J. Alloy. Compd. 771 (2019) 769–776, https://doi.org/10.1016/j.jallcom.2018.08.075.

[57] M. McHenry, M. Willard, D. Laughlin, Amorphous and nanocrystalline materials for applications as soft magnets, Prog. Mater. Sci. 44 (1999) 291–433, https://doi.org/10.1016/S0079-6425(99)00002-X.

[58] N. Khitouni, R. Daly, J. Daza, A.H. Alsulami, J.J. Suñol, M. Khitouni, Characterization of the microstructural, magnetic, and thermal behaviors of boron-doped Fe-Co-Ni alloys produced via mechanical alloying, J. Appl. Phys. 136 (2024) 35103, https://doi.org/10.1063/5.0213911.